Structural and Optical Properties of Thin Film β-Ta upon Exposure to Hydrogen to Asses Its Applicability as Hydrogen Sensing Material

Bannenberg, Lars J.; Verhoeff, Daan J.; Jonckers Newton, Nick; Thijs, Michel; Schreuders, Herman

DOI
10.1021/acsanm.3c04902

Publication date
2024

Document Version
Final published version

Published in
ACS Applied Nano Materials

ACS APPLIED NANO MATERIALS

www.acsanm.org

Article

Structural and Optical Properties of Thin Film β-Ta upon Exposure to Hydrogen to Asses Its Applicability as Hydrogen Sensing Material

Lars J. Bannenberg,* Daan J. Verhoeff, Nick Jonckers Newton, Michel Thijs, and Herman Schreuders

Cite This: *ACS Appl. Nano Mater.* 2024, 7, 1757−1766

Read Online

ACCESS | Metrics & More | Article Recommendations | Supporting Information

ABSTRACT: Here, we study the structural and optical properties of tetragonal β-tantalum-sputtered thin films both ex situ and when exposed to hydrogen, with a focus on optical hydrogen sensing applications. Using optical transmission measurements, out-of-plane and in-plane X-ray diffraction, and X-ray and neutron reflectometry, we show that thin film β-tantalum gradually, reversibly, and hysteresis-freely absorbs hydrogen with an increasing hydrogen pressure/concentration. The gradual absorption of hydrogen with increasing hydrogen concentrations induces a change in the optical transmission and reflection. These quantities change reversibly and are hysteresis-free over at least 5 orders of magnitude in hydrogen pressure/concentration, making β-tantalum a suitable hydrogen sensing material. At all partial hydrogen pressures studied, we observe that the volumetric expansion, hydrogen-to-metal ratio, and lattice expansion are substantially smaller than for body-centered cubic α-tantalum.

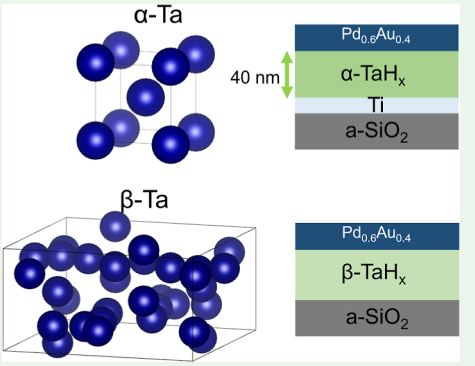

KEYWORDS: *optical hydrogen sensing, metal hydrides, thin films, tantalum, X-ray diffraction, neutron reflectometry*

1. INTRODUCTION

Tantalum and alloys thereof have recently been studied for hydrogen purification membranes,[1−5] and optical hydrogen sensing applications.[6−9] Optical hydrogen sensors rely on materials that, when exposed to a hydrogen-containing environment, absorb hydrogen and, in turn, change their optical properties. These optical properties can be probed by, e.g., measuring the optical reflectivity or transmission of the material, which is directly related to the hydrogen concentration around the sensor. Compared to conventional hydrogen sensors, optical sensors have a large and reversible hydrogen sensing range, can be made small and inexpensive, do not need the presence of oxygen, and most of all, do not require any electric currents near the sensing area, which makes them inherently safe.[10−16] This makes optical hydrogen sensors particularly attractive to sense hydrogen in a future hydrogen economy, where hydrogen sensors are essential for performance optimization in fuel cells and electrolyzers and to detect hydrogen leaks that cause safety hazards as well as indirectly contribute to the greenhouse effect.[17−23]

Body-centered cubic (bcc) tantalum (Ta), often referred to as α-Ta, and its alloys have proven to have favorable properties as a hydrogen sensing material when combined with a suitable capping layer that catalyzes hydrogen dissociation and prevents oxidation.[24] From a material perspective, thin film Ta features, unlike bulk, a large solubility of hydrogen within one thermodynamic phase and a gradual, reversible, and hysteresis-free absorption of hydrogen with increasing partial hydrogen pressure P_{H_2}, which is equivalent to an increasing hydrogen concentration c_{H_2}. The absorption of hydrogen by α-Ta at room temperature up to ~$TaH_{0.7}$ at $P_{H_2} = 10^5$ Pa results in a modest expansion of the unit cell by about 8% that is realized completely in the out-of-plane direction as a result of the clamping of the film to its support. As the films are textured with ⟨110⟩ out-of-plane, the unit cell gradually deforms upon hydrogen absorption. Surprisingly, this deformation is completely elastic, ensuring a hysteresis-free response. Combined with the monotonic changes in white-light optical transmission of α-Ta with increasing hydrogen pressure, this results in a sensing range of over 7 orders of magnitude in hydrogen pressure/concentration that is free of any hysteresis.[6−9]

Besides crystallizing in a bcc lattice, as so-called α-Ta, a metastable tetragonal form of tantalum, β-Ta has also been reported in the literature, especially for thin films.[25] Figure 1 shows that the unit cells of these polymorphs are remarkably different. Compared to the high-symmetry α-Ta [space group $Im\bar{3}m$ (229)] with a lattice constant of a = 0.330 nm, the β-Ta unit cell with lattice constants of $a = b$ = 1.02 nm and c = 0.531 nm is much larger and comprises 30 atoms. Its structure has

Received: October 14, 2023
Revised: December 29, 2023
Accepted: December 29, 2023
Published: January 16, 2024

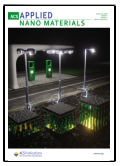

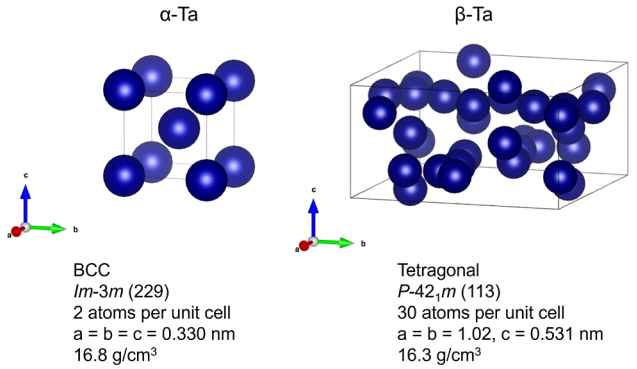

Figure 1. Unit cell and unit cell parameters of α-Ta and β-Ta. Data on α-Ta and β-Ta were adapted from refs 26 and 43, respectively. Visualizations are made with VESTA.[44]

been identified as $P\bar{4}2_1m$ (113) and results in a 3% lower density (16.3 g cm^{-3}) than α-Ta (16.8 g cm^{-3}).[26−28] We note that the very similar space group of $P4_2/mnm$ has also been linked to β-Ta.[29] In sputtered thin films, the occurrence of α/β Ta has been linked to the deposition pressure,[30] substrates temperature[30−33] and substrate or seed/adhesion layer material on which the Ta layer is grown.[32−34] Although some reports in the literature provide contradictory conclusions, the general consensus seems to be that deposition on amorphous silicon/quartz at low substrate temperatures typically results in β-Ta, while deposition on Mo, Ti, or Cr seed layers at high substrate temperatures results in the formation of α-Ta.[31−37] While many studies have been devoted to the structure and occurrence of β-Ta, to the best of our knowledge, the properties of (thin film) β-Ta under hydrogen exposure are still unknown. Detailed knowledge of these properties, as well as how the optical transmission/reflection change with exposure to hydrogen, is key when considering the use of β-Ta as a sensing material in a hydrogen sensor.

The purpose of this paper is to study the structural and optical properties of thin film β-Ta under exposure to hydrogen from the perspective of the possible applicability of the material in an optical hydrogen sensor. As illustrated in Figure 2, this sample also features a 10 nm $Pd_{0.6}Au_{0.4}$ capping

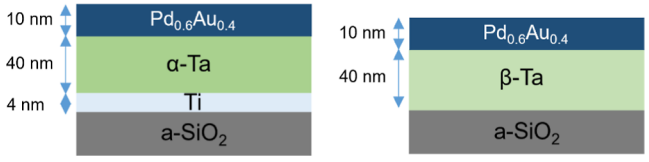

Figure 2. Schematic illustration of the two Ta samples studied in this work. The samples include a $Pd_{0.6}Au_{0.4}$ capping layer to prevent the oxidation of the Ta layer and to catalyze the dissociation of molecular hydrogen into atomic hydrogen. The α-Ta sample includes an additional Ti seed layer that promotes the growth of the α-Ta phase. The samples are grown on fused (amorphous) quartz substrates.

layer that serves to prevent oxidation of the Ta layer and catalyzes the dissociation of molecular hydrogen into atomic hydrogen. In addition, we also provide data on an α-Ta thin film that includes an additional 4 nm Ti seed layer to promote the growth of the α-Ta phase. Using in situ in-plane and out-of-plane X-ray diffraction, we establish that the unit cell only expands in the out-of-plane direction, leading to a gradual but slight elongation of the unit cell along the c-axis that is reversible, hysteresis-free, and elastic in nature. In situ X-ray and neutron reflectometry indicate that, at a given hydrogen concentration, the volumetric expansion and hydrogen-to-metal ratio of β-Ta are substantially smaller than for α-Ta. Similar to α-Ta, optical transmission measurements show a well-defined, hysteresis-free, and monotonous change of the optical transmission/reflectivity with increasing hydrogen pressure/concentration across at least 5 orders of magnitude in hydrogen pressure, making β-Ta a suitable hydrogen sensing material.

2. EXPERIMENTAL SECTION

2.1. Sample Fabrication. 40 nm α-Ta and β-Ta thin films, capped by a 10 nm $Pd_{0.6}Au_{0.4}$ layer to prevent oxidation and catalyze the hydrogen dissociation reaction, were produced by magnetron sputtering in an ultrahigh vacuum chamber (AJA Int.) with a base pressure of $P < 10^{-6}$ Pa. The reason to select $Pd_{0.6}Au_{0.4}$ instead of pure Pd as a capping layer is that alloying palladium with gold accelerates the hydrogen dissociation and substantially reduces the optical response of the capping layer.[24] To grow the 40 nm α-Ta layer, we used a 4 nm Ti adhesion/seed layer, while this layer was not deposited for the β-Ta thin film.

The layers were deposited on fused quartz substrates. For X-ray diffraction, X-ray reflectometry, and optical measurements, these substrates were 10 × 10 mm^2 in size and had a thickness of 0.5 mm and a surface roughness of <0.4 nm (Mateck GmbH, Jülich, Germany). For neutron reflectometry measurements, substrates with a diameter of 76.2 mm (3 in.), a thickness of 3.0 mm, and a surface roughness of <0.5 nm were used. All depositions were performed in 0.3 Pa of Ar, and the substrates were not heated during deposition. The deposition time, power, and rate are 114 s, 100 W DC, and 0.035 nm s^{-1} for Ti, respectively, and 292 s, 130 W DC, and 0.14 nm s^{-1} for Ta, respectively. Pd and Au were deposited simultaneously at a power of 50 and 27 W DC, respectively, for 50 s with a rate of 0.20 nm s^{-1} to achieve an atomic ratio of 60/40.

2.2. Structural Measurements. The out-of-plane and in-plane X-ray diffraction and reflectometry measurements, both ex situ and in situ, were performed using a Bruker D8 Discover (Cu Kα λ = 0.1542 nm) equipped with a LYNXEYE XE detector and operated in various configurations (Bruker AXS GmbH, Karlsruhe, Germany). For the out-of-plane X-ray diffraction and reflectometry measurements, a configuration with a Göbel mirror and a 0.2 mm exit slit on the primary side was used. On the secondary side, two 0.2 mm slits and the detector operating in 0D high count rate mode were used. For the in-plane measurements, variable slits with a footprint of 6 mm were used in combination with the detector operating in 1D high-resolution mode. In situ XRD and XRR measurements were performed in the same Anton Paar XRK900 reactor chamber (Anton Paar GmbH, Graz, Austria) connected to the same auxiliary pressure and temperature control equipment as in ref 9. In short, the partial hydrogen pressure inside this setup was varied stepwise at T = 25 °C, changing the absolute pressure of gas mixtures of 0.1% or 4.0% H_2 in He gas stepwise between 11 mbar and 6.1 bar ($\Delta c_{H_2}/c_{H_2}$ < 2%, Linde Gas Benelux BV, Dieren, The Netherlands).

In addition, in situ, in-plane XRD measurements were performed at a tilting angle χ = 65°, where the tilt was in the plane perpendicular to the X-ray beam. To perform these measurements, custom-made sample holders were designed and 3D printed with the center of rotation exactly in the center of the sample support. As these holders increased the height of the sample beyond what could be compensated by the automatic height stage of the Anton Paar reactor chamber, a 6.0 mm-thick aluminum adapter plate with a Kalrez O-ring was positioned between the sample insert and the main body of the reactor chamber.

The in situ neutron reflectometry measurements were performed at the time-of-flight neutron reflectometer ROG, located at the 2.3 MW HOR reactor of the Delft University of Technology, Delft, The Netherlands.[38] For these measurements, the same settings as the

https://doi.org/10.1021/acsanm.3c04902
ACS Appl. Nano Mater. 2024, 7, 1757−1766

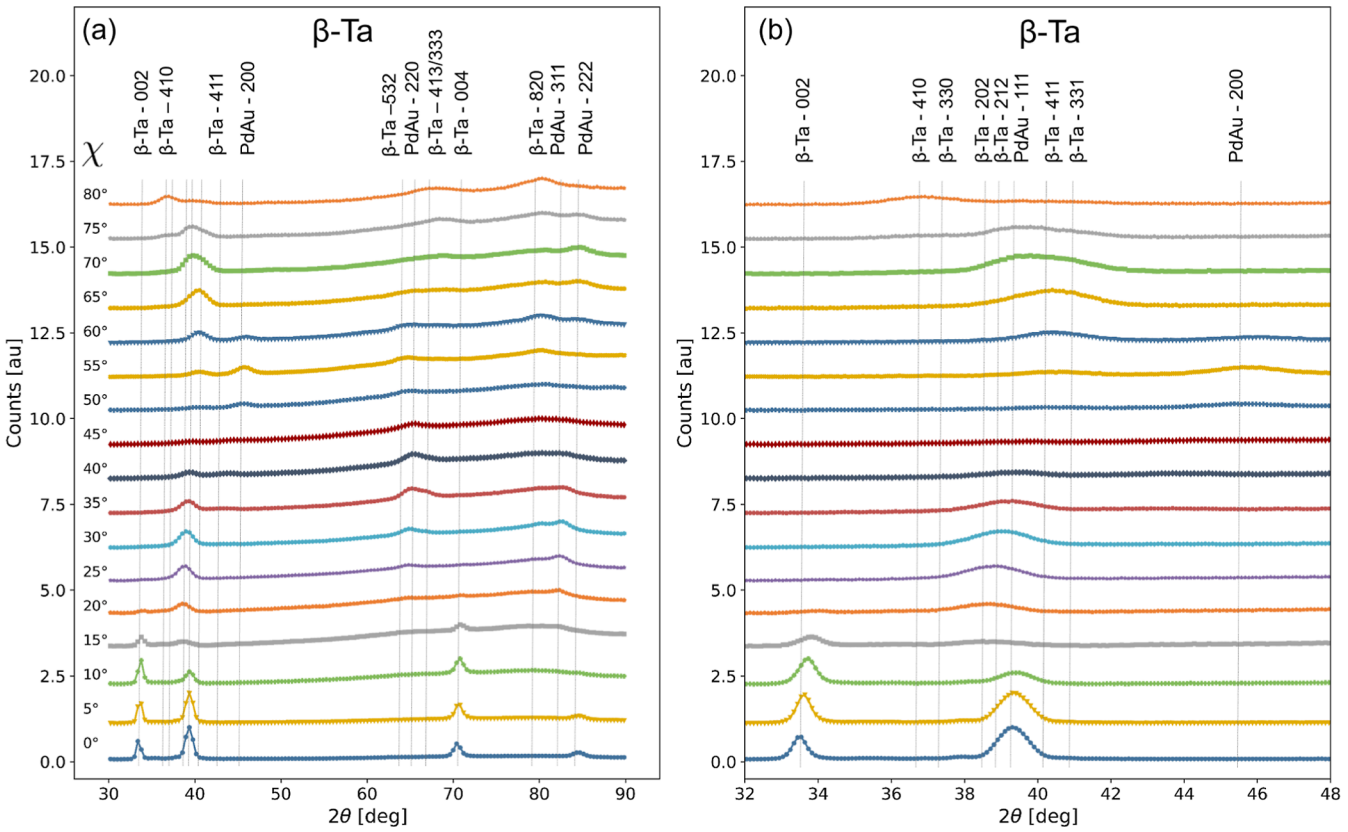

Figure 3. Out-of-plane and in-plane ex situ X-ray diffraction patterns of a thin film of 40 nm α-Ta capped with a 10 nm $Pd_{0.6}Au_{0.4}$ layer. Panel (a) shows the full pattern, and panel (b) shows a close-up for $32 \leq 2\theta \leq 48°$. χ indicates the angle at which the sample is rotated in the plane perpendicular to the X-ray beam. The X-ray diffraction patterns are normalized to the larger of 0.4 cps, or the maximum intensity of the diffraction pattern at a given χ. This is done as the intensities between the patterns measured at different values of χ strongly vary due to differences in the experimental geometry, also leading to a worsening of the resolution and broadening of the diffraction peaks.

measurements on α-Ta reported in ref 9 were used. These settings yield a footprint of 65/80 × 40 mm^2 (umbra/penumbra) and a resolution of $\Delta Q/Q \approx 5\%$. During the measurements, the sample was exposed to varying partial hydrogen pressures at $T = 22$ °C. This was done by changing the absolute pressure of gas mixtures of 0.1% or 4.0% H_2 in Ar gas between 10 mbar and 6.1 bar ($\Delta c_{H_2}/c_{H_2} < 2\%$, Linde Gas Benelux BV, Dieren, The Netherlands) in the temperature and pressure-controlled cell that is described in ref 39.

Estimates of the layer thickness, roughness, and scattering length density (SLD) for both layers were obtained by fitting the data with GenX3.[40,41] Since we are mostly interested in the Ta layer and the correlation between the thickness of the $Pd_{0.6}Au_{0.4}$ and the Ta layer is large, we fixed the thickness of the $Pd_{0.6}Au_{0.4}$ for the in situ measurements to the value obtained by fitting the as-prepared sample. Subsequently, by using the fitted values of the thickness d and SLD, we can obtain the hydrogen-to-metal ratio x using

$$x = \left(\frac{\mathrm{SLD}_{\mathrm{TaH}_x}}{\mathrm{SLD}_{\mathrm{Ta}}} \frac{d_{\mathrm{TaH}_x}}{d_{\mathrm{Ta}}} - 1 \right) \frac{b_{\mathrm{Ta}}}{b_{\mathrm{H}}} \tag{1}$$

where $\mathrm{SLD} = \sum_{i=1}^{N} b_i N_i$, with $b_{\mathrm{Ta}} = 6.91$ fm and $b_{\mathrm{H}} = -3.739$ fm, the scattering lengths of tantalum and hydrogen, respectively,[42] and N_i the number of atoms i per volume unit. As detailed in the Supporting Information, in deriving this equation, we assume that the number of metal atoms in each layer stays the same upon exposure to hydrogen and that the expansion of the film is in the out-of-plane direction only.

2.3. Optical Measurements. To measure the changes in the optical transmission and reflection as a function of hydrogen pressure/concentration, a flow setup was used. In this setup, the sample is positioned in the center of the sample chamber. This chamber has optically transparent windows on the top and bottom, i.e., below and above the sample. For the reflection measurements, two fibers are mounted at an angle of 30° with respect to the surface normal of the sample. For the transmission measurements, one optical fiber is positioned below the sample and one above. For both the reflection and transmission measurements, one of the fibers is connected to an Ocean Optics HL-2000-FSHA halogen light source (Ocean Insights Orlando, FL, United States of America), and the other one is connected to an Ocean Optics Maya2000 Pro Series Spectrometer (Ocean Insights Orlando, FL, United States of America). To adjust the intensity and spot size of the light, Thorlabs cage system iris diaphragms with a diameter of 0.8−20 mm (Thorlabs, Inc., Newton, New Jersey, United States of America) are used in combination with a lens at the end of the fiber to focus the light. The measured intensity (measured by the spectrometer) is corrected by subtracting the background signal of the spectrometer, deduced by performing a closed shutter or dark measurement.

Three mass flow controllers were used to stepwise change the partial hydrogen pressure/hydrogen concentration. These mass flow controllers have a maximum flow of 0−100, 0−200, and 0−250 SCCM (Thermal Mass GF Series, Brooks Instrument, Hatfield, PA, United States of America). The 0−250 SCCM mass flow controller is connected to the Ar gas network (5 N purity), while the other two are connected to either gas mixtures of 0.1% H_2 and 4% H_2 in Ar ($\Delta c_{H_2}/c_{H_2} < 2\%$, Linde Gas Benelux BV, Dieren, The Netherlands) or 100% H_2. The measurements are performed inside a lab with a temperature of 19.5 °C that fluctuates by ±0.5 °C.

3. RESULTS

3.1. Structural Measurements. *3.1.1. Ex Situ Measurements.* As a first step, we verify with out-of-plane and in-plane

https://doi.org/10.1021/acsanm.3c04902
ACS Appl. Nano Mater. 2024, 7, 1757−1766

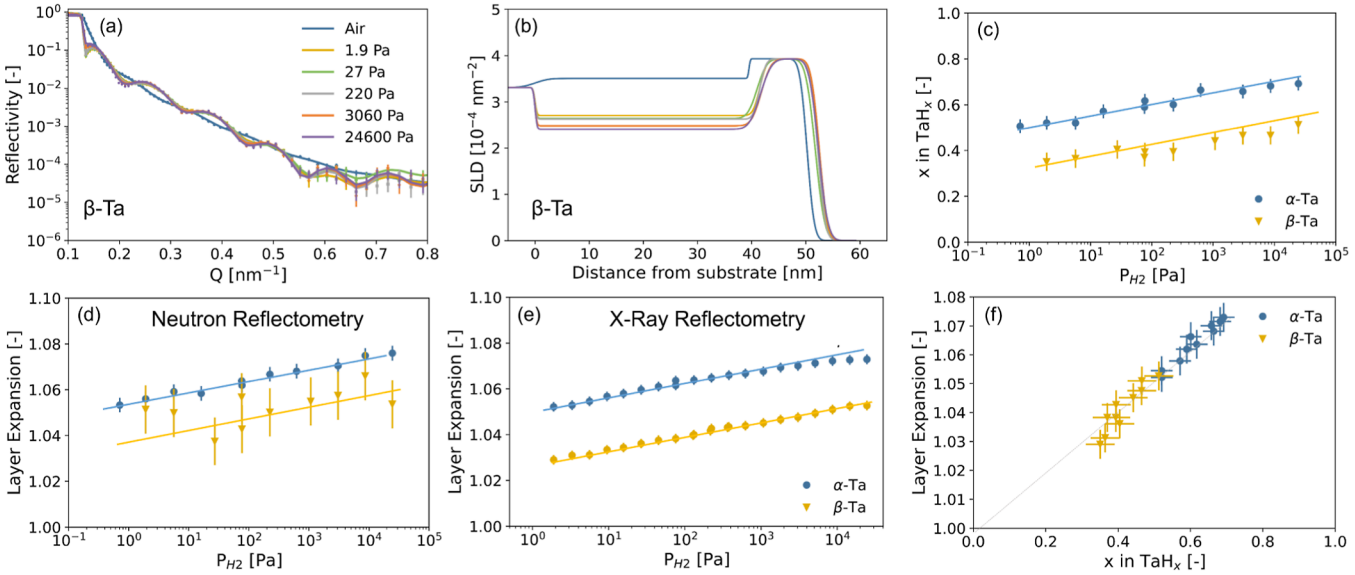

Figure 4. Neutron and X-ray reflectometry results at T = 22 °C of a thin film of 40 nm β-Ta capped with a 10 nm $Pd_{0.6}Au_{0.4}$ layer. Data on α-Ta is adapted from ref 9 Panel (a) shows the neutron reflectometry data as measured under the partial hydrogen pressures indicated. The continuous lines represent the fit of the model to the data. (b) Corresponding SLD profiles. The X-ray reflectograms and corresponding SLD profiles are available in Figure S2. (c) Hydrogen-to-metal ratio of the Ta layer as a function of the partial hydrogen pressure computed following eq 1 and using the SLD and thickness obtained from fitting the neutron reflectometry data. (d) Ta layer expansion was obtained from neutron reflectometry as a function of the partial hydrogen pressure. (e) Ta layer expansion was obtained from X-ray reflectometry as a function of the partial hydrogen pressure. (f) Layer expansion as obtained from X-ray reflectometry as a function of the hydrogen-to-metal ratio. The continuous lines in panels (c–f) serve as guides to the eye.

XRD whether the synthesized films have the expected crystal structure. The out-of-plane measurements correspond to an XRD measurement in a Bragg–Brentano configuration where the sample is positioned on a flat sample stage and the X-ray source and detector synchronously move around the sample. Differently, during the in-plane measurements, the sample is rotated stepwise by an angle χ in the plane perpendicular to the X-ray beam to probe in-plane lattice vectors while the X-ray source and detector synchronously move to vary 2θ. Figure 3 shows the results for the sample with a 40 nm Ta layer and a 10 nm $Pd_{0.6}Au_{0.4}$ layer. For the out-of-plane measurements (χ = 0°), we see that the sample shows four reflections: two correspond to the (111) and (222) reflections of the $Pd_{0.6}Au_{0.4}$ capping layer at 2θ = 39.3, 84.6°, and two reflections at 2θ = 33.5, 70.4° correspond to the (002) and (004) reflections of β-Ta. This indicates that the sample is strongly textured with (002) in the out-of-plane direction, as other even more intense reflections like (413) do not appear.

To increase the confidence that the sample is indeed β-Ta, in-plane measurements ($\chi \neq 0°$) are performed. In these measurements, the sample is tilted in steps of 5° in the plane perpendicular to the X-ray beam by $0° \leq \chi \leq 80°$, while at each χ-position, a diffraction pattern is measured between $30° \leq 2\theta \leq 90°$. The in-plane measurements are consistent with the β-Ta structure. Indeed, the most intense reflections of this structure (see Tables S1 and S2 for an overview) show up at the expected tilting angle χ and 2θ positions. For example, the (413) reflection at 2θ = 40.2° occurs at χ = 65°, which is expected given that the angle between (002) and (413) is 65.3°. As a comparison, we find that for the sample with an additional 4 nm Ti adhesion/seed layer, the structure corresponds to α-Ta (Figure S1).

3.1.2. In Situ Reflectometry. As the next step, we study if and how β-Ta responds to the presence of hydrogen. From a structural perspective, the ideal hydrogen sensing material has (i) a gradual hydrogenation of the material across a wide partial hydrogen pressure range/hydrogen concentration range to ensure a large sensing range, (ii) a large solubility range of hydrogen within one thermodynamic phase without any (first-order) phase transition to ensure a reversible and hysteresis-free response, and (iii) a limited volumetric expansion to ensure a stable response over repeated exposure to hydrogen.

First, we use neutron reflectometry to determine how much hydrogen is absorbed by β-Ta as a function of the partial hydrogen pressure and compare it with previous measurements from ref 9 on α-Ta. This is obtained by fitting the measured neutron reflectometry data of Figure 4a to a two-layer model for the β-Ta thin film: one layer is for the β-Ta layer, and one layer is for the $Pd_{0.6}Au_{0.4}$ capping layer. For each of these layers, a thickness, roughness, and SLD are obtained that can be graphically represented in the SLD plot of Figure 4b. This SLD is affected by the absorption of hydrogen and, together with the thickness of the layer, can be used to calculate the hydrogen-to-metal ratio of the layer (see eq 1 and the Supporting Information), reported in Figure 4c. The expansion of the layer determined from neutron reflectometry is reported in Figure 4d.

Two important conclusions from the data presented in Figure 4 can be drawn: first, the results indicate a gradual hydrogenation of β-Ta with an increasing partial hydrogen pressure. For hydrogen sensing applications, this is beneficial as it potentially allows for a wide partial hydrogen/hydrogen concentration range in which the sensor can determine the hydrogen concentration. Additionally, the window in which the hydrogenation occurs at room temperature is beneficial, as P_{H_2} = 4000 Pa is equivalent to c_{H_2} = 4% in air, i.e., the explosive limit of hydrogen–air mixtures, and a wide range of concentrations can be probed around this value. Second, we

https://doi.org/10.1021/acsanm.3c04902
ACS Appl. Nano Mater. 2024, 7, 1757–1766

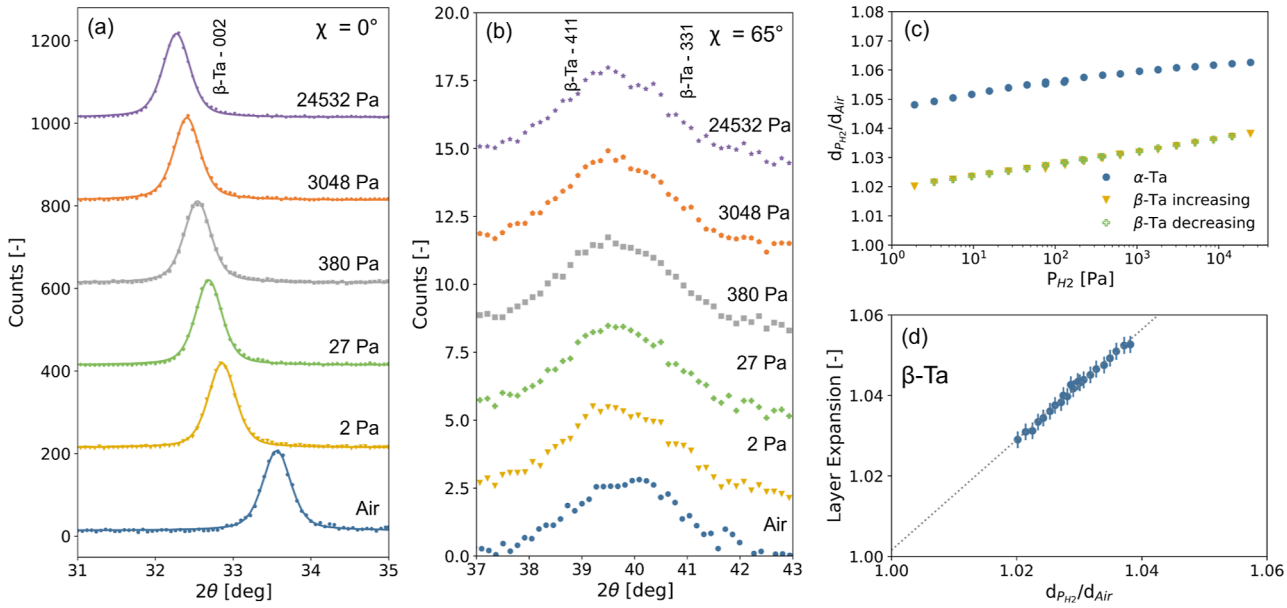

Figure 5. In situ out-of-plane and in-plane X-ray diffraction results at T = 25 °C of a thin film of 40 nm β-Ta capped with a 10 nm $Pd_{0.6}Au_{0.4}$ layer. Data on α-Ta is adapted from ref 9 (a) Out-of-plane X-ray diffraction measurements around the (002) reflection as measured under the partial hydrogen pressures indicated and by stepwise increasing the pressure. The continuous lines represent a fit of a pseudo-Voigt function to the data to deduce the d-spacing. (b) In-plane in situ X-ray diffraction measurement measured at $\chi = 65°$. (c) d_{002} spacing as a function of the partial hydrogen pressure as compared with α-Ta and between increasing and decreasing steps. (d) Ta layer expansion obtained from X-ray reflectometry as a function of the expansion of the out-of-plane d_{002} expansion.

find that β-Ta absorbs substantially less hydrogen at a given hydrogen pressure than α-Ta. At P_{H_2} = 24,600 Pa, α-Ta has a hydrogen-to-metal ratio of $x \approx 0.7$, while β-Ta has a hydrogen-to-metal ratio of $x \approx 0.5$.

Corresponding to the smaller hydrogen-to-metal ratio, we also find a much smaller layer expansion for β-Ta than α-Ta at any given partial hydrogen pressure. This can be seen in Figure 4d for the layer thickness derived from the neutron reflectometry. However, due to the poor contrast between the substrate and the Ta layer for β-Ta (the additional Ti layer for α-Ta ensures sufficient contrast in SLD), the uncertainty is large. For this reason, we also performed XRR measurements (Figure S2), for which the derived layer expansion is reported in Figure 4e. These XRR measurements show that at P_{H_2} = 24,600 Pa, the highest partial hydrogen at which we measured and at which the hydrogen-to-metal ratio is $x \approx 0.5$, the thickness of the β-Ta layer is about 5% larger than when the film is not exposed to hydrogen. This is substantially less than the 7% expansion observed for α-Ta ($x \approx 0.7$).

As such, we observe that the expansion obtained from XRR is indeed different than the values obtained from NR (see Figure S3) and that the error on the expansion deduced from XRR is, as expected, much smaller than for NR. The systematic deviation is likely the result of the relatively large absolute error on the thickness of the Ta layer in air, where the neutron SLD contrast with the substrate was minimal. As this value is used to compute the expansion at each partial hydrogen pressure, this can lead to a systematic deviation between the thickness derived from the XRR and NR data. We note that the expansion/thickness is also used to compute the hydrogen-to-metal ratio (see eq 1). Using the thickness derived from XRR instead of the thickness derived from neutron reflectometry resulted in a maximum difference of Δx = 0.03.

In addition, we note that the absorption of hydrogen causes the roughness of the Ta−$Pd_{0.6}Au_{0.4}$ to reversibly increase from about 1 nm when no hydrogen is absorbed (i.e., in air) to 2 nm at the largest hydrogen pressure. This increase is likely related to the expansion of the layer and, as we will see, the deformation of the unit cell. Owing to correlations between the fitted parameters in reflectometry (thickness, SLD, and roughness), this changing roughness may increase the uncertainty of the fitted parameters, especially for the NR results where the SLD contrast is relatively limited and the Q-range is smaller than for XRR. As such, it provides a further explanation of the difference in expansion determined based on NR and XRR.

Most importantly, Figure 4f plots the layer expansion for both α and β-Ta as a function of the hydrogen-to-metal ratio x and indicates that the layer expansion is proportional to the amount of hydrogen absorbed by the layer. In addition, this proportionality is the same for both α and β-Ta, indicating that the volume the Ta host lattice expands for a given hydrogen-to-metal ratio x is irrespective of the crystal structure. This observation is thus consistent with an elastic deformation of the Ta unit cell.[9]

3.1.3. In Situ X-ray Diffraction. Next, we applied X-ray diffraction to study whether the unit cell of β-Ta (i) gradually expands or (ii) has any phase transition. In particular, we use these results to determine if the expansion of the material is free of any hysteresis. Unlike in bulk, for which a series of phase transitions have been reported as a function of the hydrogen-to-metal ratio at room temperature, an extensive solid-solution range is found in α-Ta thin films up to at least $x \approx 0.7$. The expansion of the α-Ta films is realized in the out-of-plane direction only (i.e., ⟨110⟩), causing the unit cell to gradually deform. To the best of our knowledge, no data on the crystal structure of β-TaH_x upon exposure to hydrogen has been reported.

Figure 5 depicts the in situ out-of-plane diffraction patterns for the β-Ta film, focusing on the (002) reflection. As can be

https://doi.org/10.1021/acsanm.3c04902
ACS Appl. Nano Mater. 2024, 7, 1757−1766

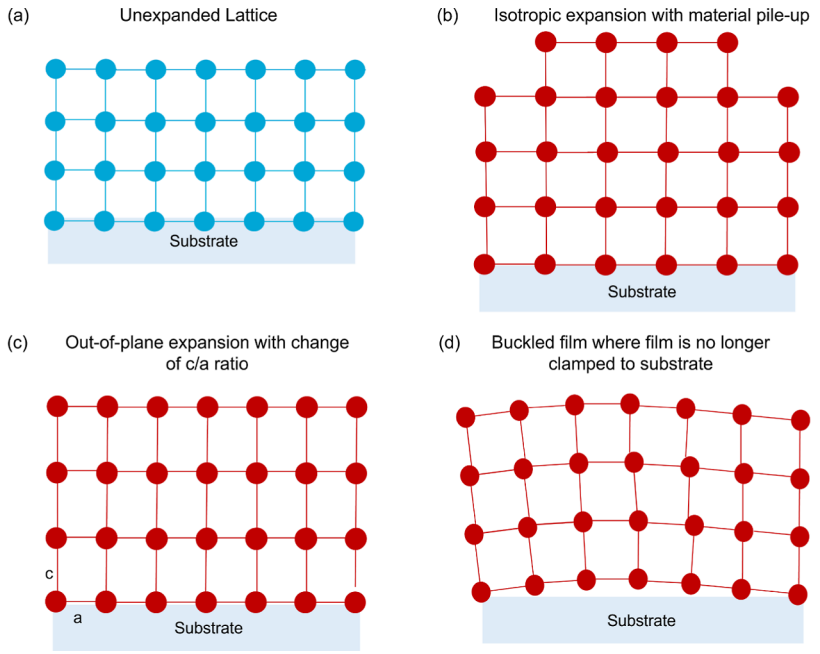

Figure 6. Schematic illustration of an (a) unexpanded lattice (no exposure to hydrogen) and (b–d) three possible scenarios that could occur when the lattice expands to accommodate hydrogen. The dots indicate the lattice points. The figure is not to scale, and a cubic lattice is selected for simplicity as the unexpanded lattice.

seen, with increasing partial hydrogen pressure, a gradual shift of the diffraction peak to lower diffraction angles occurs. This implies, according to Bragg's law, $n\lambda = 2d_{hkl}\theta_{hkl}$, a gradual expansion of the d_{002} spacing with increasing hydrogen pressure. Importantly, we do not observe any coexistence or widening of the peak, which is consistent with the absence of any phase transition. Also, the in-plane in situ XRD results at $\chi = 65°$ are consistent with the absence of any phase transition as no additional reflection appears. Indeed, despite the poor resolution, no indication of a significant peak shape change is observed, as well as no additional reflection appears or no reflection disappears.

By fitting the peak to a pseudo-Voight function to extract the peak position and applying Bragg's law, we obtain the d_{002} spacing as a function of hydrogen pressure. Figure 5c shows the d_{002} expansion relative to the d_{002} spacing measured in air as a function of the partial hydrogen pressure. Two important conclusions can be derived from it: First, the out-of-plane lattice expansion of α-Ta is much larger than that of β-Ta. This is consistent with the lower hydrogen-to-metal ratio and layer expansion at any given partial hydrogen pressure (Figure 4). Second, we find that the d_{002} expansion is the same at any given partial hydrogen pressure after increasing and decreasing the pressure steps. This is an important observation, as it implies that there is no hysteresis, which is particularly important for optical hydrogen sensing applications as it ensures that the output of the hydrogen sensor is the same, irrespective of the pressure history of the sensor. The absence of hysteresis is also consistent with the absence of any phase transition.

As a next step in our analysis, we plot the layer expansion as a function of the out-of-plane d_{002} spacing expansion. For a clamped thin film, the volumetric expansion is proportional to the layer thickness expansion. In the case of isotropic expansion, we would expect that the volumetric expansion $\frac{V_{PH_2}}{V_{air}}$ of the material as a result of the hydrogenation is given by

$$\frac{V_{PH_2}}{V_{air}} = \frac{d_{100,PH_2}}{d_{100,air}}\frac{\Delta d_{010,PH_2}}{d_{010,air}}\frac{\Delta d_{002,PH_2}}{d_{002,air}} \quad (2)$$

where $\frac{\Delta d_{hkl}}{d_{hkl}}$ is the relative expansion of the d_{hkl} spacing. As illustrated schematically in Figure 6b, in this scenario, more atoms/unit cells need to be stacked on top of each other as fewer unit cells fit in a certain plane. Differently, when the expansion is completely out-of-plane, i.e., in the [002] direction, $\frac{d_{100,PH_2}}{d_{100,air}}$ and $\frac{\Delta d_{010,PH_2}}{d_{010,air}}$ are both 1 and eq 2 reduces to

$$\frac{V_{PH_2}}{V_{air}} = \frac{\Delta d_{002,PH_2}}{d_{002,air}} \quad (3)$$

In this scenario, the number of unit cells per plane remains the same (Figure 6c).

To examine which of these two scenarios is applicable, Figure 5d depicts the layer expansion as a function of the out-of-plane d_{002} spacing expansion and indeed shows a linear relationship between the layer expansion and $\frac{\Delta d_{hkl}}{d_{hkl}}$. As such, and similar to α-Ta, we can conclude that the expansion of the lattice is completely in the out-of-plane direction. Additional support for this conclusion is provided by the fact that the in-plane XRD results at $\chi = 65°$ do not show a substantial 2θ shift with increasing partial hydrogen pressure (Figure 5c). As such, the c/a ratio of the unit cell is continuously altered as a function of hydrogen pressure, and the unit cell deforms. However, the absence of any hysteresis in the d_{002}-expansion and the proportionality between the layer expansion and hydrogen-to-metal ratio indicate that this deformation is completely elastic in nature and not plastic.

A third effect that could happen is that the film buckles and is no longer completely clamped to the substrate (Figure 6d). While we know that the film did not completely delaminate from the substrate, as this would not lead to neutron or X-ray reflectometry data that can be analyzed with the present two-

https://doi.org/10.1021/acsanm.3c04902
ACS Appl. Nano Mater. 2024, 7, 1757–1766

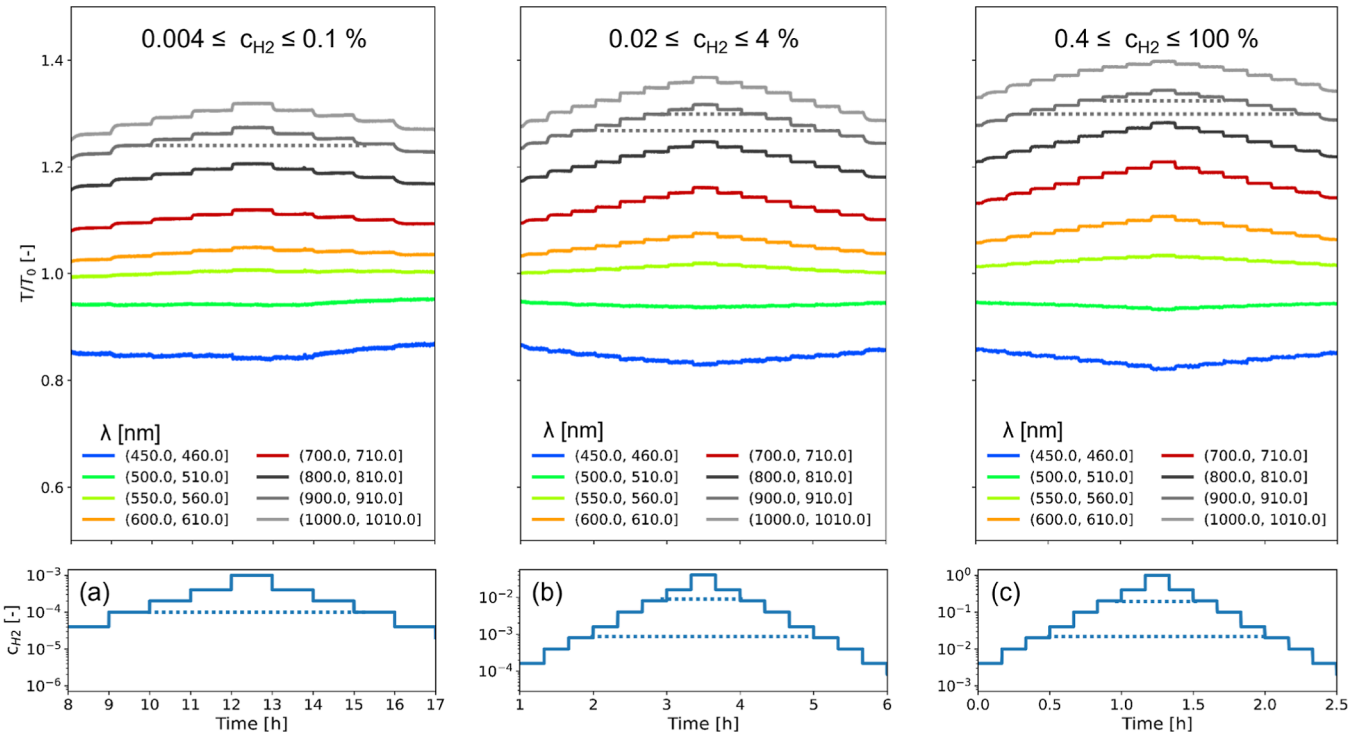

Figure 7. Optical transmission of a 40 nm β-Ta thin film capped by a 10 nm $Pd_{0.6}Au_{0.4}$ capping layer relative to the transmission of the as-prepared film as a function of time during which the hydrogen concentration was stepwise changed in the regimes (a) $0.004 \leq c_{H_2} \leq 0.1\%$, (b) $0.02 \leq c_{H_2} \leq 4\%$, and (c) $0.4 \leq c_{H_2} \leq 100\%$. The dashed lines indicate levels of the same transmission (top panel) and hydrogen concentration (bottom panel).

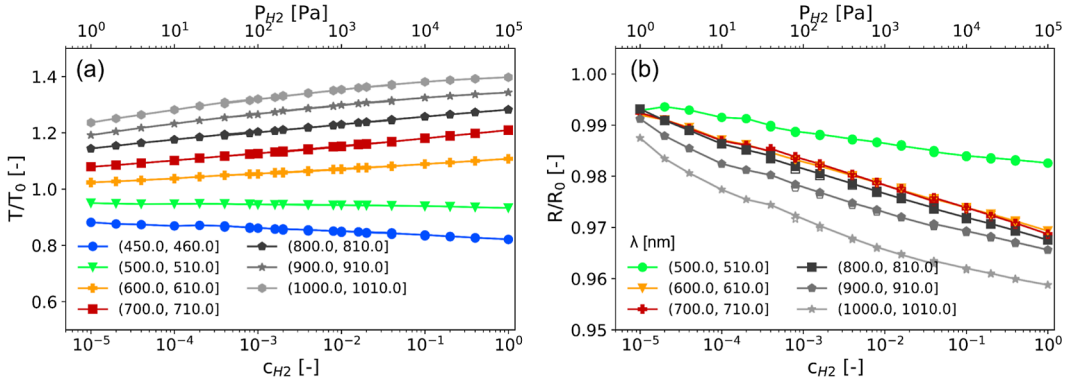

Figure 8. Optical (a) transmission and (b) reflection of a 40 nm β-Ta thin film capped by a 10 nm $Pd_{0.6}Au_{0.4}$ capping layer relative to the transmission/reflection of the as-prepared film as a function of the hydrogen concentration (at 1 atm) and the partial hydrogen pressure for the wavelength bins indicated. The closed and open symbols indicate the value of the transmission/reflection after increasing and decreasing pressure steps, respectively.

layer model, local buckling could occur. To test this, we performed a rocking curve around the critical edge of the X-ray reflectogram. The data (Figure S5) show a slight broadening of the rocking curve when the film is exposed to hydrogen. This could indicate that the expansion as a result of the hydrogen absorption induces partial/limited buckling of the sample. However, this may also arise from other effects due to the bending of the substrate due to high stress. Furthermore, a rocking curve around the (002) diffraction peak indicates that the preferred orientation of the sample remains unaffected (Figure S6).

3.2. In Situ Optical Measurements. As a next step, we evaluate how the optical properties change as a function of applied hydrogen pressure. To do this, we mix various hydrogen-containing gases (100% H_2 and 0.1% and 4% H_2 gas mixtures in Ar) with pure Ar at a constant pressure of 1 bar to stepwise vary the hydrogen concentration to which the sample is exposed. Figure 7 shows the optical transmission, normalized to the transmission of the film when no hydrogen was present, of several wavelengths as a function of time and in three hydrogen concentration regimes.

Three important conclusions can be derived from Figure 7. First of all, we observe well-defined, stable, and clear steps in the optical transmission that reflect the changes in the hydrogen concentration. It indicates that the optical properties of the material are significantly and monotonically altered when the hydrogen concentration is changed, a prerequisite for an effective hydrogen sensing material. Second, we see that the optical response is the same at a given hydrogen concentration after an increase or decrease in the hydrogen pressure. This

https://doi.org/10.1021/acsanm.3c04902
ACS Appl. Nano Mater. 2024, 7, 1757−1766

absence of hysteresis, consistent with the absence of a phase transition, the absence of plastic deformation, and the absence of hysteresis in the d_{002}-spacing, is important for optical hydrogen sensing applications as it makes the sensor not only reversible but also provides a response irrespective of the hydrogen concentration history. Third, we see that the response of the optical transmission to a change in hydrogen concentration has a different direction and magnitude depending on the optical wavelength. For example, for near-infrared light (λ = 900 nm), we observe a strong increase with increasing hydrogen concentration, while a decrease is observed for blue light (λ = 450 nm).

To summarize the changes in optical transmission as a function of hydrogen concentration, we plotted in Figure 8a the optical transmission as a function of the hydrogen concentration for multiple wavelengths. This plot is obtained by averaging the optical transmission in Figure 8 at each step in hydrogen concentration over the last minute of the step. In this plot, the open symbols reflect the average optical transmission after a decrease in the hydrogen concentration, while the closed symbols show the optical transmission after an increase in the hydrogen concentration. The results confirm our previous observations regarding a monotonous, substantial, and hysteresis-free response of the optical transmission as a function of hydrogen concentration. Indeed, for hydrogen concentrations of $0.001 \leq c_{H_2} \leq 100\%$, i.e., across at least 5 orders of magnitude in hydrogen concentration, we observe a monotonous change in the optical transmission. Furthermore, we see that these changes are positive for orange, red, and infrared light, indicating that the sample becomes more transparent for these wavelengths, while the optical changes are negative for blue and green light, indicating that the sample becomes more opaque when exposed to hydrogen. This is further illustrated in Figure S4, which shows the total optical transmission change at c_{H_2} = 100% relative to the sample measured in air. Such opposite responses of the transmission/reflection for different wavelengths to hydrogen facilitate the use of an algorithm that can be used to determine the hydrogen concentration with higher sensitivity and reduced drift.[45] Moreover, we find that not only the optical transmission but also the optical reflectivity change monotonously with increasing hydrogen concentration (Figure 8b).

An aspect not discussed so far is the selectivity of the hydrogen sensor material, that is, if the optical response is solely induced by the presence of hydrogen and is not affected by the presence of any other chemical species. While not primarily the focus of this work, metal-hydride sensors, relying on the absorption of hydrogen, have the advantage that they are, in principle, not sensitive to other combustible gases, which is the case for other types of hydrogen sensors. However, the catalyst layer responsible for the dissociation of molecular hydrogen into atomic hydrogen, in this case $Pd_{0.6}Au_{0.4}$, also provides protection against, e.g., oxidation. This layer can be poisoned by the presence of other chemical species such as CO, CO_2, and NO_X. To prevent deactivation of this layer, one can alloy it with, e.g., Cu for CO protection[14] or add an additional polymeric layer on top of the $Pd_{0.6}Au_{0.4}$ layer, such as poly(methyl methacrylate) or polytetrafluoroethylene.[46,47]

4. CONCLUSIONS

In conclusion, using optical transmission measurements, out-of-plane and in-plane X-ray diffraction, and X-ray and neutron reflectometry, we show that $Pd_{0.6}Au_{0.4}$-capped β-tantalum thin films gradually, reversibly, and hysteresis-freely absorb hydrogen with an increasing hydrogen pressure/concentration. Neutron and X-ray reflectometry show that with increasing partial hydrogen pressure/concentration, the hydrogen-to-metal ratio increases gradually. At any given partial hydrogen pressure/concentration, the hydrogen-to-metal ratio and layer expansion are substantially smaller than for α-Ta. Furthermore, X-ray diffraction indicates the absence of any phase transition and that the expansion with increasing hydrogen-to-metal ratio of the unit cell is realized completely in the out-of-plane direction. These structural properties are reflected in the changes in the optical transmission and reflectivity, which change reversibly and hysteresis-free over at least 5 orders of magnitude in hydrogen pressure/concentration, making β-tantalum a suitable hydrogen sensing material.

■ ASSOCIATED CONTENT

Supporting Information

The Supporting Information is available free of charge at https://pubs.acs.org/doi/10.1021/acsanm.3c04902.

Section on determining the hydrogen-to-metal ratio from neutron reflectometry, in-plane ex situ measurements of a 40 nm α-Ta thin film capped by a 10 nm $Pd_{0.6}Au_{0.4}$ layer, tables with expected diffraction reflection for α-Ta, β-Ta, and $Pd_{0.6}Au_{0.4}$, X-ray reflectometry measurements and corresponding scattering length density profiles, and changes in optical transmission as a function of a wavelength between the sample measured in air and at P_{H_2} = 0.1 MPa (PDF)

■ AUTHOR INFORMATION

Corresponding Author

Lars J. Bannenberg − *Faculty of Applied Sciences, Delft University of Technology, 2629 JB Delft, The Netherlands;* orcid.org/0000-0001-8150-3694; Email: l.j.bannenberg@tudelft.nl

Authors

Daan J. Verhoeff − *Faculty of Applied Sciences, Delft University of Technology, 2629 JB Delft, The Netherlands*

Nick Jonckers Newton − *Faculty of Applied Sciences, Delft University of Technology, 2629 JB Delft, The Netherlands*

Michel Thijs − *Faculty of Applied Sciences, Delft University of Technology, 2629 JB Delft, The Netherlands*

Herman Schreuders − *Faculty of Applied Sciences, Delft University of Technology, 2629 JB Delft, The Netherlands*

Complete contact information is available at: https://pubs.acs.org/10.1021/acsanm.3c04902

Notes

The authors declare no competing financial interest.

■ ACKNOWLEDGMENTS

Raymon Bresser, Piet van der Ende, and Kees de Vroege are warmly thanked for their support with the neutron reflectometry measurements. Bart Boshuizen is greatly thanked for designing and maintaining Labview software to control the

pressure cells. Erwin Janssen and Jörg Haberlah are thanked for providing the gas cylinders.

REFERENCES

(1) Rothenberger, K. S.; Howard, B. H.; Killmeyer, R. P.; Cugini, A. V.; Enick, R. M.; Bustamante, F.; Ciocco, M. V.; Morreale, B. D.; Buxbaum, R. E. Evaluation of tantalum-based materials for hydrogen separation at elevated temperatures and pressures. *J. Membr. Sci.* **2003**, *218*, 19−37.
(2) Ockwig, N. W.; Nenoff, T. M. Membranes for hydrogen separation. *Chem. Rev.* **2007**, *107*, 4078−4110.
(3) Dolan, M. D. Non-Pd BCC alloy membranes for industrial hydrogen separation. *J. Membr. Sci.* **2010**, *362*, 12−28.
(4) Nozaki, T.; Hatano, Y.; Yamakawa, E.; Hachikawa, A.; Ichinose, K. Improvement of high temperature stability of Pd coating on Ta by HfN intermediate layer. *Int. J. Hydrogen Energy* **2010**, *35*, 12454−12460.
(5) Pal, N.; Agarwal, M.; Maheshwari, K.; Solanki, Y. S. A review on types, fabrication and support material of hydrogen separation membrane. *Mater. Today: Proc.* **2020**, *28*, 1386−1391.
(6) Bannenberg, L. J.; Boelsma, C.; Schreuders, H.; Francke, S.; Steinke, N.-J.; Van Well, A. A.; Dam, B. Optical Hydrogen Sensing Beyond Palladium: Hafnium and Tantalum as Effective Sensing Materials. *Sens. Actuators, B* **2019**, *283*, 538−548.
(7) Bannenberg, L. J.; Schreuders, H.; Dam, B. Tantalum-Palladium: Hysteresis-Free Optical Hydrogen Sensor over 7 Orders of Magnitude in Pressure with Sub-Second Response. *Adv. Funct. Mater.* **2021**, *31*, 2010483.
(8) Bannenberg, L. J.; Schreuders, H.; van Beugen, N.; Kinane, C.; Hall, S.; Dam, B. Tuning the properties of thin film TaRu for hydrogen sensing applications. *ACS Appl. Mater. Interfaces* **2023**, *15*, 8033−8045.
(9) Bannenberg, L. J.; Blom, L.; Sakaki, K.; Asano, K.; Schreuders, H. Completely elastic deformation of hydrogenated Ta thin films. *ACS Mater. Lett.* **2023**, *5*, 962−969.
(10) Hübert, T.; Boon-Brett, L.; Black, G.; Banach, U. Hydrogen Sensors−a Review. *Sens. Actuators, B* **2011**, *157*, 329−352.
(11) Wadell, C.; Syrenova, S.; Langhammer, C. Plasmonic Hydrogen Sensing with Nanostructured Metal Hydrides. *ACS Nano* **2014**, *8*, 11925−11940.
(12) Bannenberg, L. J.; Boelsma, C.; Asano, K.; Schreuders, H.; Dam, B. Metal Hydride Based Optical Hydrogen Sensors. *J. Phys. Soc. Jpn.* **2020**, *89*, 051003.
(13) Bannenberg, L. J.; Heere, M.; Benzidi, H.; Montero, J.; Dematteis, E. M.; Suwarno, S.; Jaroń, T.; Winny, M.; Orłowski, P. A.; Wegner, W.; Starobrat, A.; Fijałkowski, K. J.; Grochala, W.; Qian, Z.; Bonnet, J. P.; Nuta, I.; Lohstroh, W.; Zlotea, C.; Mounkachi, O.; Cuevas, F.; Chatillon, C.; Latroche, M.; Fichtner, M.; Baricco, M.; Hauback, B. C.; El Kharbachi, A. Metal (boro-) Hydrides for High Energy Density Storage and Relevant Emerging Technologies. *Int. J. Hydrogen Energy* **2020**, *45*, 33687−33730.
(14) Darmadi, I.; Nugroho, F. A. A.; Langhammer, C. High-Performance Nanostructured Palladium-Based Hydrogen Sensors−Current Limitations and Strategies for Their Mitigation. *ACS Sens.* **2020**, *5*, 3306−3327.
(15) Koo, W.-T.; Cho, H.-J.; Kim, D.-H.; Kim, Y. H.; Shin, H.; Penner, R. M.; Kim, I.-D. Chemiresistive Hydrogen Sensors: Fundamentals, Recent Advances, and Challenges. *ACS Nano* **2020**, *14*, 14284−14322.
(16) Chen, K.; Yuan, D.; Zhao, Y. Review of Optical Hydrogen Sensors Based on Metal Hydrides: Recent Developments and Challenges. *Opt Laser. Technol.* **2021**, *137*, 106808.
(17) Brandon, N. P.; Kurban, Z. Clean Energy and the Hydrogen Economy. *Philos. Trans. R. Soc., A* **2017**, *375*, 20160400.
(18) Dusastre, V. Hydrogen to the Rescue. *Nat. Mater.* **2020**, *17*, 565.
(19) Abe, J. O.; Popoola, A. P. I.; Ajenifuja, E.; Popoola, O. M. Hydrogen Energy, Economy and Storage: Review and Recommendation. *Int. J. Hydrogen Energy* **2019**, *44*, 15072−15086.
(20) Glenk, G.; Reichelstein, S. Economics of Converting Renewable Power to Hydrogen. *Nat. Energy* **2019**, *4*, 216−222.
(21) Bakenne, A.; Nuttall, W.; Kazantzis, N. Sankey-Diagram-based Insights into the Hydrogen Economy of Today. *Int. J. Hydrogen Energy* **2016**, *41*, 7744−7753.
(22) El Kharbachi, A.; Dematteis, E. M.; Shinzato, K.; Stevenson, S. C.; Bannenberg, L. J.; Heere, M.; Zlotea, C.; Szilágyi, P. Á.; Bonnet, J.-P.; Grochala, W.; et al. Metal Hydrides and Related Materials. Energy Carriers for Novel Hydrogen and Electrochemical Storage. *J. Phys. Chem. C* **2020**, *124*, 7599−7607.
(23) Warwick, N.; Griffiths, P.; Keeble, J.; Archibald, A.; Pyle, J.; Shine, K. Atmospheric implications of increased Hydrogen use. Avaliable at: https://assets.publishing.service.gov.uk/government/uploads/system/uploads/attachment_data/file/1067144/atmospheric-implications-of-increased-hydrogen-use.pdf, 2022; p 75, (accessed Dec 4, 2023).
(24) Bannenberg, L. J.; Boshuizen, B.; Ardy Nugroho, F. A.; Schreuders, H. Hydrogenation kinetics of metal hydride catalytic layers. *ACS Appl. Mater. Interfaces* **2021**, *13*, 52530−52541.
(25) Read, M. H.; Altman, C. A new structure in tantalum thin films. *Appl. Phys. Lett.* **1965**, *7*, 51−52.
(26) Arakcheeva, A.; Chapuis, G.; Grinevitch, V. The self-hosting structure of β-Ta. *Acta Crystallogr., Sect. B: Struct. Sci.* **2002**, *58*, 1−7.
(27) Jiang, A.; Yohannan, A.; Nnolim, N. O.; Tyson, T. A.; Axe, L.; Lee, S. L.; Cote, P. Investigation of the structure of β-tantalum. *Thin Solid Films* **2003**, *437*, 116−122.
(28) Lee, S. L.; Doxbeck, M.; Mueller, J.; Cipollo, M.; Cote, P. Texture, structure and phase transformation in sputter beta tantalum coating. *Surf. Coat. Technol.* **2004**, *177−178*, 44−51.
(29) Moseley, P. T.; Seabrook, C. The crystal structure of β-tantalum. *Acta Crystallogr., Sect. B: Struct. Crystallogr. Cryst. Chem.* **1973**, *29*, 1170−1171.
(30) Schauer, A.; Roschy, M. R.F. sputtered β-tantalum and b.c.c. tantalum films. *Thin Solid Films* **1972**, *12*, 313−317.
(31) Zhou, Y. M.; Xie, Z.; Xiao, H. N.; Hu, P. F.; He, J. Effects of deposition parameters on tantalum films deposited by direct current magnetron sputtering. *J. Vac. Sci. Technol., A* **2009**, *27*, 109−113.
(32) Nasakina, E. O.; Sevostyanov, M. A.; Mikhaylova, A. B.; Baikin, A. S.; Sergienko, K. V.; Leonov, A. V.; Kolmakov, A. G. Formation of alpha and beta tantalum at the variation of magnetron sputtering conditions. *IOP Conf. Ser.: Mater. Sci. Eng.* **2016**, *110*, 012042.
(33) Colin, J. J.; Abadias, G.; Michel, A.; Jaouen, C. On the origin of the metastable β-Ta phase stabilization in tantalum sputtered thin films. *Acta Mater.* **2017**, *126*, 481−493.
(34) Abadias, G.; Colin, J. J.; Tingaud, D.; Djemia, P.; Belliard, L.; Tromas, C. Elastic properties of α- and β-tantalum thin films. *Thin Solid Films* **2019**, *688*, 137403.
(35) Chen, G. S.; Chen, S. T.; Huang, S. C.; Lee, H. Y. Growth mechanism of sputter deposited Ta and Ta−N thin films induced by an underlying titanium layer and varying nitrogen flow rates. *Appl. Surf. Sci.* **2001**, *169−170*, 353−357.
(36) Zhang, J.; Huai, Y.; Chen, L.; Zhang, J. Formation of low resistivity alpha Ta by ion beam sputtering. *J. Vac. Sci. Technol., B: Microelectron. Nanometer Struct.–Process., Meas., Phenom.* **2003**, *21*, 237−240.
(37) Bernoulli, D.; Müller, U.; Schwarzenberger, M.; Hauert, R.; Spolenak, R. Magnetron sputter deposited tantalum and tantalum nitride thin films: An analysis of phase, hardness and composition. *Thin Solid Films* **2013**, *548*, 157−161.
(38) Bannenberg, L. J.; Bresser, R.; van der Ende, P.; van Exter, M.; van Goozen, W.; Naastepad, F.; Thijs, M. A.; Verleg, M. N.; de Vroege, K.; Waaijer, R.; van Well, A. A. The completely renewed and upgraded neutron reflectometer at the TU Delft Reactor Institute. *Rev. Sci. Instrum.* **2023**, *94*, 111501.
(39) Bannenberg, L. J.; van Exter, M.; Verleg, M.; Boshuizen, B.; Parnell, S.; Thijs, M.; Schreuders, H. Versatile pressure and temperature controlled cell for neutron reflectometry and small-angle neutron scattering. *J. Neutron Res.* **2023**, *26*, 1−13.

https://doi.org/10.1021/acsanm.3c04902
ACS Appl. Nano Mater. 2024, 7, 1757−1766

(40) Björck, M.; Andersson, G. GenX: an Extensible X-ray Reflectivity Refinement Program Utilizing Differential Evolution. *J. Appl. Crystallogr.* **2007**, *40*, 1174−1178.
(41) Glavic, A.; Björck, M. GenX 3: the latest generation of an established tool. *J. Appl. Crystallogr.* **2022**, *55*, 1063−1071.
(42) Sears, V. F. Neutron scattering lengths and cross sections. *Neutron news* **1992**, *3*, 26−37.
(43) Vavilova, V. V.; Galkin, L. N.; Glazov, M. V. Stabilization of a Phase With the delta-Mn Structure by Rapid Quenching in the Rhenium−Tantalum System. *Dokl. Akad. Nauk SSSR* **1988**, *300*, 1157−1161.
(44) Momma, K.; Izumi, F. VESTA: a three-dimensional visualization system for electronic and structural analysis. *J. Appl. Crystallogr.* **2008**, *41*, 653−658.
(45) Bannenberg, L. J. Algorithm to suppress drift for micro-mirror and other intensity modulated hydrogen sensors. *IEEE Sens. J.* **2023**, *23*, 30720−30727.
(46) Ngene, P.; Westerwaal, R. J.; Sachdeva, S.; Haije, W.; de Smet, L. C. P. M.; Dam, B. Polymer-Induced Surface Modifications of Pd-based Thin Films Leading to Improved Kinetics in Hydrogen Sensing and Energy Storage Applications. *Angew. Chem., Int. Ed.* **2014**, *53*, 12081−12085.
(47) Nugroho, F. A. A.; Darmadi, I.; Cusinato, L.; Susarrey-Arce, A.; Schreuders, H.; Bannenberg, L. J.; da Silva Fanta, A. B.; Kadkhodazadeh, S.; Wagner, J. B.; Antosiewicz, T. J.; Hellman, A.; Zhdanov, V. P.; Dam, B.; Langhammer, C. Metal-Polymer Hybrid Nanomaterials for Plasmonic Ultrafast Hydrogen Detection. *Nat. Mater.* **2019**, *18*, 489−495.

https://doi.org/10.1021/acsanm.3c04902
ACS Appl. Nano Mater. 2024, 7, 1757−1766